Structural and transport properties of quenched and melt-spun BixSb2–xTe3 solid solutions (x = 0.40 and 0.48)

Viktoriia Ohorodniichuk, Soufiane El-Oualid, Anne Dauscher, Christophe Candolfi, Philippe Masschelein, Sylvie Migot, Pascal Dalicieux, Philippe Baranek, Bertrand Lenoir

Structural and transport properties of quenched and melt-spun $Bi_xSb_{2-x}Te_3$ solid solutions (x = 0.40 and 0.48)

Viktoriia Ohorodniichuk[1], Soufiane El-Oualid[1], Anne Dauscher[1], Christophe Candolfi[1], Philippe Masschelein[1], Sylvie Migot[1], Pascal Dalicieux[2], Philippe Baranek[3], **Bertrand Lenoir**[1,*]

[1] *Université de Lorraine, CNRS, Institut Jean Lamour, 2 allée André Guinier, Campus ARTEM, F-54000 Nancy, France*

[2] *EDF R&D, Department TREE, EDF Lab Les Renardières, Avenue des Renardières – Ecuelles, 77818 Moret-sur-Loing Cedex, France*

[3] *EDF R&D, Department EFESE, EDF Lab Paris-Saclay, 7 boulevard Gaspard Monge, 91120 Palaiseau, France*

[*] Corresponding author: bertrand.lenoir@univ-lorraine.fr

Abstract

We report on a detailed investigation of the structural and transport properties of $Bi_xSb_{2-x}Te_3$ (x = 0.40 and 0.48) samples, prepared by either water quenching or melt-spinning (MS) and consolidated by spark plasma sintering (SPS), by means of X-ray diffraction, scanning and transmission electron microscopy, and transport property measurements (5 – 480 K). All the samples crystallize in the rhombohedral structure type of Bi_2Te_3. While the samples prepared by water quenching exhibit some segregations of the elements over the micron length scale, the MS samples are highly homogeneous. Unlike prior reports where an increase in the

dimensionless thermoelectric figure of merit *ZT* has been observed in MS samples, we find that both series of samples show similar peak *ZT* values. Owing to slight variations in the hole concentration, the maximum *ZT* is shifted closer to room temperature in MS samples with a peak *ZT* of 1.1 achieved at 340 K for $x = 0.48$. Our results highlight the extreme sensitivity of the *ZT* values to the Bi content and, for a given chemical composition, to slight variations in the hole concentration and microstructure. We further demonstrate the good reproducibility of the MS technique indicating that this method enables controlling the defect concentration inherent to these materials.

Keywords: thermoelectric; melt-spinning; bismuth telluride

Introduction

Due to its unique advantages such as high reliability, no emissions of toxic gases, long lifetime and absence of moving parts, solid-state thermoelectric energy conversion has gained a renewed interest over the last decades [1-3]. This versatile technology offers the possibility to cool or heat systems or to produce electricity directly from any heat source. The potential of a given material to convert a thermal gradient into electrical energy (or vice-versa) at a given absolute temperature *T* is determined by the so-called dimensionless thermoelectric figure of merit *ZT* defined as $ZT = \frac{\alpha^2}{\rho\kappa}T = \frac{P}{\kappa}T$ where α is the thermopower (or Seebeck coefficient), ρ is the electrical resistivity, κ is the total thermal conductivity, and $P = \frac{\alpha^2}{\rho}$ is the power factor [4,5].

Following the early developments of semiconductors in the 1950s, Bi_2Te_3-based alloys were identified to be suitable materials for thermoelectric applications near room temperature

[6,7]. Even after decades of intensive research activities, these materials still remain nowadays the reference thermoelectric materials in commercial devices. Bi_2Te_3, along with its solid solutions with Sb_2Te_3 and Bi_2Se_3, belong to the class of narrow-band-gap semiconductors that crystallize in the $R\bar{3}m$ space group. The best *p*-type thermoelectric properties are achieved in the Sb_2Te_3-rich solid solutions $Bi_xSb_{2-x}Te_3$ for $x \sim 0.4 – 0.5$ with a peak *ZT* of around 0.9 – 1.0 near 300 K in commercial materials [7].

Over the past few years, several studies have reported *ZT* values substantially higher than unity in these *p*-type compounds. Most of these advances have been attributed to the beneficial influence of nanostructuration, achieved by various synthesis methods [6]. Along this line, the most impressive improvements in thermoelectric properties were obtained by applying the melt-spinning (MS) technique [8-11]. *ZT* values as high as 1.56 at 300 K were reported in a series of studies, making MS an innovative route for developing high performance Bi_2Te_3-based alloys. These studies followed pioneering works performed in the 1980s and 1990s on the binaries Bi_2Te_3, Sb_2Te_3 and Bi_2Se_3 prepared by MS [12-16]. Even if these remarkable values have been tempered recently with *ZT* values close to 1.1 – 1.2 [17-24], all the studies showed that MS is a worthwhile mean for further optimizing the thermoelectric performances of Sb_2Te_3 and Bi_2Te_3-based materials near room temperature.

As the thermoelectric properties are strongly sensitive to the Bi content in these alloys, several attempts at investigating the influence on the thermoelectric properties of the Bi-to-Sb ratio of the initial ingot for MS have been performed [11,22,25]. These studies have evidenced that **i)** the best composition falls within the range $0.4 \leq x \leq 0.5$, and **ii)** the thermoelectric performances achieved are significantly improved in MS samples compared to standard zone-leveling ingots. In a prior study on the melt-spun $Bi_{0.48}Sb_{1.52}Te_3$ ribbons themselves, we showed that they are highly-textured and exhibit more pronounced metallic transport properties with respect to samples of similar chemical compositions prepared by conventional powder

metallurgy, that is, quenched from the melt followed by fast sintering by spark plasma sintering [20]. A direct comparison between samples prepared by quenching in room-temperature water and by MS could provide additional information on the exact impact of the MS process on the transport properties, which are not directly accessible by a comparison to zone-leveling-prepared polycrystals.

Here, we address this as-yet unexplored issue via a detailed investigation of the structural, electrical, thermal and galvanomagnetic properties (5 – 473 K) of $Bi_xSb_{2-x}Te_3$ with x = 0.40 and 0.48 prepared by water-quenching and MS. The similar chemical compositions of both series of samples allowed for a systematic comparison of the transport properties, thereby clearly highlighting the influence of the MS process. In addition, the anisotropy on the electrical and thermal transport and its evolution with temperature has been assessed by measurements on samples cut parallel and perpendicular to the pressing direction. This point is pivotal to determining the most favorable direction and evaluating correctly the *ZT* values. Measurements performed on different batches of MS samples demonstrate that our preparation process leads to highly-reproducible results with a maximum *ZT* value of 1.1 achieved at 340 K in the MS x = 0.48 sample.

Experimental details

Synthesis

The synthesis of the initial ingots was performed from high-purity (5N +, 99.999%) Bi, Te and Sb elements in the form of granules. Stoichiometric amounts of these elements for the targeted $Bi_xSb_{2-x}Te_3$ (x = 0.40 and 0.48) compositions were placed in cleaned and degassed silica tubes of 15 mm inner diameter. The tubes were sealed under an argon-hydrogen

atmosphere (95/5%), placed in a vertical rocking furnace, heated to 983 K for 5 h, finally followed by quenching in room-temperature water. The resulting ingots were cut in pieces that were subsequently used either to prepare reference samples or as the starting material for the melt-spinning process. The reference samples were obtained by hand-grinding the ingot into fine powders that were consolidated by spark plasma sintering (SPS) under a pressure of 30 MPa at 773 K for 5 min. The consolidated cylinders were 7 mm in height and 10 mm in diameter with a relative density, determined by weight and geometrical dimensions, higher than 97 %. The melt-spinning process was applied to the ingot using an Edmond Bühler apparatus under the following conditions: heating at 883 K, copper wheel of 19.8 cm in diameter rotating at 36 $m.s^{-1}$ linear speed and an argon overpressure of 0.8 bar. The nozzle diameter of the quartz tube was set to 1 mm as it showed to be the best experimental diameter to obtain enhanced thermoelectric properties [18]. The obtained melt-spun ribbons were hand-crushed and further densified by SPS under the same conditions used for the reference samples. More details on the preparation method can be found in [18-20]. Hereafter, the four synthesized samples will be labelled as Ref0.40, Ref0.48, MS0.40 and MS0.48 for the reference and MS samples, respectively, with 0.40 and 0.48 referring to the Bi content x in $Bi_xSb_{2-x}Te_3$.

Structural and chemical characterizations

Powder X-ray diffraction (PXRD) was used to assess the phase purity of the four samples (Bruker-D8 Advance diffractometer, $CuK\alpha_1$ radiation, λ = 1.54056 Å, 300 K). The chemical homogeneity and morphology of the samples was probed by scanning electron microscopy (SEM) ((FEI-Quanta FEG 650) on polished (back-scattered mode: BSE) and fractured (secondary electrons mode: SE) samples, respectively. The chemical compositions were determined by wavelength dispersive X-ray spectroscopy (WDXS) (JEOL-J7600F instrument)

using Bi, Sb and PbTe as standards for determining the concentrations of Bi, Sb and Te, respectively. Around 100 points were measured on each samples. The micro-nanostructure of the bulk MS samples has been observed by transmission electron microscopy (TEM) (JEOL-CM200) on thin slices obtained by micro-cleavage and deposited on a carbon-covered copper grid.

Transport properties measurements

The thermoelectric and galvanomagnetic properties were measured along (that is, parallel) or perpendicular to the pressing direction to probe the anisotropy. Several samples were cut with a diamond wire saw from the dense SPS samples into bar, disk and/or square-shaped samples (typical dimensions of 2.5×2×8 mm^3, Ø = 10 mm and 6×6×1 mm^3, respectively) as illustrated in Figure 1. Measurements in both directions are critical in mixed Sb_2Te_3-Bi_2Te_3 polycrystals since an erroneous combination of transport properties measured along different directions can lead to an overestimation of *ZT* of up to 100% due to the significant anisotropy in the transport properties.

Low-temperature thermoelectric properties (2 – 300 K) were measured using the thermal transport option (TTO) of the physical properties measurement system (PPMS, Quantum Design) on the bar-shaped samples. The contacts were realized by soldering four copper leads onto the sample using a low-melting-point braze. Hall coefficient measurements were conducted between 5 and 300 K on the same sample using the AC transport option of the PPMS. A five-probe method was utilized by soldering copper wires to the sample with the same low-melting-point braze. Transverse electrical resistivity ρ_{xy} data were collected while sweeping the magnetic field $\mu_0 H$ from −1 up to +1T. The data were corrected to dismiss possible magnetoresistive contribution due to contacts misalignment following the formula $\rho_H =$

$[\rho_{xy}(+\mu_0 H) - \rho_{xy}(-\mu_0 H)]/2$ where ρ_H is the Hall voltage. Specific heat was measured on a small square-shaped sample (mass of ~ 15 mg) from 2 to 300 K using the dedicated option of the PPMS.

High-temperature thermoelectric measurements were carried out in the 300 – 500 K temperature range. Thermopower and electrical resistivity were measured simultaneously with a ZEM3 system (ULVAC-RIKO) under helium atmosphere on the bar-shaped samples. Thermal diffusivity *a* was determined in the same temperature range using a Netzsch laser flash instrument (LFA 427). The samples (cylinder or square-shaped samples) were coated on both sides with a thin layer of graphite to optimize absorption of the laser shot and emission. The data were analyzed by the Cowan model including pulse correction. The specific heat C_p was measured by differential scanning calorimetry (DSC Netzsch Pegasus) on small cylinder-shaped samples. Assuming a constant density ρ_V, the thermal conductivity κ was calculated from $\kappa = a\rho_V C_p$.

An overall good match between the low- and high-temperature data sets was observed, the deviation being at most 10% at 300 K. The combined uncertainty in the determination of *ZT* is estimated to be ~ 17% [26].

Results and discussion

Microstructure and chemical homogeneity

As the Sb_2Te_3-Bi_2Te_3 pseudo-binary phase diagram shows a solid solution with liquidus and solidus lines separated by a temperature of around 5 K for x = 0.4 and 0.48, both $Bi_{0.4}Sb_{1.6}Te_3$ and $Bi_{0.48}Sb_{1.52}Te_3$ compounds do not melt congruently [27]. Thus, chemical segregations are possible in the initial ingots obtained from a rapid solidification of the melt

during water quenching. This possibility was checked on the quenched ingots by EDXS. These analyses revealed the presence of micro-segregations of Bi and Sb elements in the ingot suggesting that the cooling rate achieved by water quenching, estimated to be between 600 – 1200 K s^{-1}, is too low to yield a homogenous bulk material. However, as shown below, these inhomogeneities do not have any significant effect on the MS samples.

The PXRD patterns of the four different samples (Ref and MS samples with x = 0.40 and 0.48) are shown in Figure 2a. Both Ref and MS samples are well crystallized, with all the observed peaks corresponding to the rhombohedral $R\bar{3}m$ crystal structure of $Bi_{0.5}Sb_{1.5}Te_3$ (indexed according to Pearson's crystal data, powder pattern n°310785). A magnification of the main peak (015) highlights the displacement of the peak position towards lower angles for the Ref0.48 and MS0.48 samples with respect to the 0.40 samples (Figure 2b). This trend is consistent with the larger atomic radius of Bi (R_{Bi} = 1.63 Å) compared to that of Sb (R_{Sb} = 1.53 Å). MS samples exhibit broader peaks than the Ref samples due to the reduced grain size, as expected from the MS process.

Figure 3 shows SEM images taken on polished and fractured SPS samples. In good agreement with the peak broadening observed by PXRD, the MS samples show smaller grain sizes compared to the corresponding reference samples (10-15 μm versus < 2 μm, see fracture images on Fig. 3). The grain size in the MS samples is smaller than that reported by Zheng et *al*. (about 8.8 μm) despite a similar speed of the copper roller [17]. Our values are, however, consistent with those determined by Deng et *al*. [22,23]. Similar to what has been observed by all these authors, no preferred orientation could be detected upon closer inspection of the grains that show a lamellar structure. Both reference samples exhibit some phase contrast in backscattered electron images, with features appearing as compositional stripes oriented perpendicular to the pressing direction. For example, compositions varying from $Bi_{0.36}Sb_{1.60}Te_{3.04}$ to $Bi_{0.50}Sb_{1.47}Te_{3.03}$ (observed in the whiter places) have been determined by

WDXS analyses performed on the Ref0.40 sample. It is interesting to note that the SPS process improves the chemical homogeneity of the initial water-quenched ingots, despite the presence of these compositional stripes. The origin of such original features is however not fully understood. One possibility is that they originate from the micro-segregations observed in the water-quenched ingot which are not fully suppressed by the SPS process. In contrast, the chemical homogeneity of the MS samples after SPS is excellent with no obvious Te-rich phases detectable. This result can be attributed to the very high cooling rate undergone by the melt during the MS process that leads to homogeneous ribbons, as shown in our previous study [20].

The average actual compositions, determined by WDXS analyses and normalized to 5 atoms per formula unit, were measured by averaging about 90 measurement points (Table 1). A good correlation between the nominal and actual compositions is observed for the Ref and MS samples. Further insights into the variations in composition all over the surface can be obtained by sorting out the data according to an increase in the Bi content, as exemplified in Fig. 4 for the x = 0.40 sample. Although the Bi content corresponds to the expected concentration for nearly all the points, a small excess is nevertheless observed for about 15 points, which is to the detriment of the Sb content. Moreover, the actual Sb content is systematically lower than the nominal value leading to an increased Te content (Table 1, Fig. 4).

Figure 5 shows TEM images collected on two different micro-cleaved fragments that are typical of what could be observed on several fragments of the MS0.40 sample. The micron-sized particles seen by SEM in the MS samples could not be observed by TEM since thin enough large fragments were not achieved with the micro-cleavage technique. On one hand, grains of about several hundreds of nm are visible (Fig. 5b). On the other hand, some fragments clearly display features indicative of closely packed, seemingly aggregated nano-grains with no amorphous structure (Fig. 5a). The electron diffraction pattern taken on these fragments

exhibits nearly bright continuous diffraction rings that could all be indexed within the $R\bar{3}m$ space group of $Bi_{0.4}Sb_{1.6}Te_3$. By selecting spots on two different rings, the corresponding dark field images highlight the presence of the diffracting nanoparticles. Their size is less than 20 nm, confirming that the MS process is an efficient way to preserve nano-particles and that the SPS process does not significantly affect the size of these nanoparticles. The densely-packed nano-grains form a large number of grain boundaries that can impede the movement of dislocations [28] and significantly affect phonon scattering, ultimately enhancing the thermoelectric properties.

Transport properties

The temperature dependence of the electrical resistivity ρ of the reference and MS $Bi_xSb_{2-x}Te_3$ samples for x = 0.40 and 0.48 are shown in Figures 6a and 6b, respectively. Measurements were performed parallel and perpendicular to the pressing direction. For the reference samples, the ρ values are constant below T < 20 K and increase with increasing temperature above this temperature. Taking into account the magnitude of ρ (from 2 to 24 μΩ.m), this behavior is typical of heavily-doped semiconductors. We note that ρ is anisotropic for both x = 0.40 and 0.48 with values significantly higher in the pressing direction than in the perpendicular direction. Furthermore, the anisotropy ratio (ρ_{par}/ρ_{perp}) increases with temperature to reach 1.4 and 1.7 at 300 K for x = 0.40 and 0.48, respectively. This feature, in line with the results obtained on single crystals [29], indicates that the SPS process induces a preferred orientation along the direction of the applied SPS pressure. Increasing the Bi content from x = 0.40 to x = 0.48 results in a slight increase in ρ in both directions.

Although the MS samples show similar general trends compared to the reference samples (Figs 6a and 6b), a noticeable difference can be observed: the anisotropy ratio is significantly

lower in the x = 0.40 and 0.48 samples, with values close to 1 between 300 and 460 K. This result is in good agreement with the aforementioned structural analyses.

The temperature dependence of the Hall coefficient R_H, measured between 5 and 300 K, is shown in Fig. 7. All the samples exhibit a smooth temperature dependence, with a slight increase upon warming. This behavior is in good agreement with those obtained on single crystals [29-32], for which, an increase in the Hall coefficient was explained using a two valence-band model. For all samples, R_H is positive indicating that the electrical transport is dominated by holes. The R_H values of the x = 0.40 and x = 0.48 Ref and MS samples are very close in both directions suggesting that R_H is nearly isotropic. However, we should stress here that some anisotropy may nevertheless exist as reported by Gerovac et *al*. [33] on polycrystalline samples prepared by mechanical alloying. The reason comes from the fact that two Hall coefficients are present in $Bi_xSb_{2-x}Te_3$ single crystals due to their layered crystal structure: R_{123} and R_{231} (in this notation the first index refers to the direction of the electrical field, the second to the direction of the current and the third one to the direction of the magnetic field; the numbers 1, 2 and 3 referring to the binary, bisectrix and trigonal axis, respectively). Stördeur et *al*. [34] showed that these two coefficients are not equal in single crystals in the low field limit ($\mu B << 1$ where μ is the carrier mobility and B is the magnetic field) due to the peculiarities of the valence band structure. In addition, the difference between these two coefficients depends on the composition, that is, on the x value. For x = 0.40, the difference at 300 K was found to be only about 9% but can be as high as 34% for x = 1 [34]. Based on these considerations, it cannot be strictly ruled out that a difference exists between the Hall coefficients measured on samples cut perpendicular (where roughly $R_{H\text{-}perp} \sim R_{123}$) or parallel (where roughly $R_{H\text{-}par} \sim R_{231}$) to the pressing direction.

Following several prior investigations, the hole concentration can be determined from R_H assuming a single-parabolic-band model. In this approximation, the (apparent) hole

concentration p is simply defined by $p = \frac{1}{R_H e}$ where e is the elementary charge. In single crystals, the Hall coefficient $R_H = R_{123}$, corresponding to a magnetic field along the trigonal axis and a current and Hall field along the basal planes, is usually used. In polycrystalline samples, the orientation closest to this configuration is obtained in samples cut perpendicular to the pressing direction. For this reason, we used $R_{H\text{-}perp}$ for the calculation of p.

Within this approximation, the temperature dependence of p was inferred and is shown in Figure 8. p is constant below 20 K and decreases slowly between 20 and 200 K. In Ref0.40 and Ref0.48 samples, p is equal to 3.9×10^{19} cm^{-3} and 3.6×10^{19} cm^{-3} at 300 K, respectively. The MS process does not seem to strongly impact the hole concentration even though no clear trend emerges from these data. While p increases in the x = 0.40 sample (4.8×10^{19} cm^{-3} at 300 K), it decreases for x = 0.48 (2.4×10^{19} cm^{-3} at 300 K). In our previous study, we showed that the MS ribbons for x = 0.48 exhibit a more pronounced metallic character ($p \sim 9\times10^{19}$ cm^{-3}) compared to the reference sample, presumably due to extra holes associated with Te vacancies [20]. The results obtained herein show that the consolidation of the ground ribbons by SPS reduces the initial charge carrier concentration. A possible scenario could be that the Te precipitates observed in the ribbons dissolve into the matrix during the SPS treatment, thereby reducing p. Regardless of the synthetic process used, the x = 0.40 sample exhibits higher p than x = 0.48. This behavior can be explained qualitatively if we assume, as in single crystals, that holes are mainly created in bulk polycrystals by antisite defects which originate from the substitution of Bi or Sb for Te atoms with the driving force to create such defects being the small difference of electronegativity between these atoms. Hence, increasing the Bi_2Te_3 content should lead to a lower amount of antisite defects due to the larger difference in electronegativity between Bi and Te with respect to Sb and Te.

From the Hall and electrical resistivity measurements, the Hall mobility along the perpendicular direction $\mu_H = R_H/\rho$ can be calculated (Fig. 9). At 300 K, the μ_H values reach

nearly 200 $cm^2\ V^{-1}\ s^{-1}$ in the reference samples, which are comparable to those observed in single crystals of the same composition [27]. Near 300 K, μ_H follows a $T^{-3/2}$ dependence and saturates to a constant value below about 15 K. This behavior is suggestive of a combination of scattering by neutral impurities below 15 K while acoustic phonon scattering dominates at higher temperatures. These trends are similar in the MS samples, even though the values, while still large, are somehow degraded by the MS process due to differences in the microstructure.

The thermopower α is shown as a function of temperature in Fig. 10. All the samples show positive α values, which vary linearly from 5 to 40 K. Above this temperature, α increases logarithmically with T up to 300 K. Above 300 K, the slope of $\alpha(T)$ decreases, vanishes and eventually becomes negative for some samples. This behavior is consistent with the thermal excitation of minority carriers across the band gap. As a consequence, the higher the hole concentration, the higher the temperature at which the samples enter the intrinsic regime. From this simple picture, we can safely conclude that the MS0.48 sample has the lowest hole concentration, which is consistent with Hall effect data. From the position of the maximum α value (α_{max}), the band gap energy E_g (in eV) can be estimated from the formula derived by Goldsmid and Sharp [35], $E_g = 2e\alpha_{max}T_{max}$ where T_{max} is the absolute temperature at which α_{max} occurs. Taking α_{max} = 220 $\mu V.K^{-1}$ at T_{max} = 420 K for the MS0.48 sample yields E_g = 185 meV. This value is in excellent agreement with those determined using more sophisticated techniques [36,37]. The lower α values measured in the MS0.40 sample compared to the MS0.48 sample are consistent with a higher hole concentration in the former.

The α data also evidence the absence of anisotropy below 300 K in the reference samples. At higher temperatures, however, the values measured in the parallel direction exceed those measured perpendicular to the pressing direction (the maximum anisotropy ratio is around 10%). In Sb_2Te_3-rich $Bi_xSb_{2-x}Te_3$ single crystals, α can be anisotropic depending on the carrier concentration with values along the trigonal axis being higher than those perpendicular to it,

possibly due to an anisotropy in the effective masses [29]. Considering that our reference samples show some degree of texture as evidenced by the electrical resistivity, an anisotropy in α is thus possible. Interestingly, this anisotropy is suppressed over the entire temperature range in the MS samples.

The temperature dependence of the total thermal conductivity κ for the reference and MS samples is shown in Fig. 11. Upon warming, $\kappa(T)$ increases with increasing temperature following approximately a T dependence, shows a maximum near 20 K and then decreases smoothly up to 350 – 400 K depending on the samples before eventually increasing again. At 300 K, the κ value of the samples measured in the perpendicular direction ranges between 1.2 and 1.6 W m^{-1} K^{-1}. Another clear evidence of the anisotropy in the Ref samples is provided by a comparison of the thermal conductivity measured in both directions. The anisotropy ratio $\kappa_{perp}/\kappa_{par}$ is around 1.3 – 1.5 at 300 K and is higher for x = 0.48 than for x = 0.40. This ratio evolves with temperature and peaks near the highest κ value for which $\kappa_{perp}/\kappa_{par}$= 1.6 – 1.7. Of note, the anisotropy ratio is opposite to that of the electrical resistivity, similar to what has been widely observed in single crystals. No evidence of anisotropy in the MS samples seems to emerge from these data (Fig. 11b). This result is consistent with the conclusions drawn from the ρ data and in agreement with the conclusions of Xie et *al.* [38], who reported for the composition x = 0.48, an anisotropy of 2 – 3% for samples sintered by SPS at a pressure of 30 MPa. κ of the MS samples does not show any clear trend compared to the reference samples. The enhancement of κ above 350 – 400 K, which is sample dependent, is due to an additional contribution of electron-hole pairs to the thermal conduction as a result of the excitation of minority carriers across the band gap. The temperature at which this bipolar contribution occurs matches well the temperature at which α starts decreasing.

Based on these results, the temperature dependence of ZT is shown for all samples in Fig. 12. The bell-shaped peak observed near room temperature in the $ZT(T)$ curves is characteristic

of these *p*-type ternary compounds. For the reference samples, maximum *ZT* values of 1.1 (x = 0.4) and 1.05 (x = 0.48) are achieved near T = 400 K in samples cut parallel to the pressing direction. The MS samples show similar thermoelectric performances in both directions. The peak *ZT* of 1.1 is shifted to 340 K in the MS0.48 sample while the MS0.40 sample shows a slightly lower peak *ZT* value of 0.9 due to the increased hole concentration in this sample. These results highlight the strong sensitivity of *ZT* to small variations in the chemical composition and, for a given composition, to small variations in the carrier concentration and microstructure.

Of note, although we do observe interesting thermoelectric performances for one MS composition (x = 0.48), our findings contrast substantially with the results of Xie et *al*. [8,10,11,38], who reported *ZT* values higher than 1.2 at 300 K for $0.4 \leq x \leq 0.52$ with a maximum of 1.5 for x = 0.48. The reasons behind such discrepancies are yet to be understood. Nevertheless, several studies have recently reported experimental results for this family of materials prepared by MS that are in better agreement with our results [17,21-24,39-41].

Because various methods used to prepare *p*-$Bi_xSb_{2-x}Te_3$ ternary compounds often led to thermoelectric properties that were not reproducible, it is essential to determine the robustness of the experimental protocol described herein to produce MS samples. In this context, we prepared two MS samples (x = 0.48) coming from two distinct batches and characterized their electronic and thermal properties along and perpendicular to the pressing direction. The transport and galvanomagnetic data obtained on these samples, gathered in Fig. 13, demonstrate the good reproducibility of the techniques used to fabricate these materials. In each case, the deviations observed in the transport properties are below few percent. These results further show that MS provides a fruitful approach to optimize and control the thermoelectric properties of these technologically-important chalcogenides.

Summary and conclusions

We have synthesized polycrystalline and melt-spun $Bi_xSb_{2-x}Te_3$ samples for $x = 0.40$ and $x = 0.48$ consolidated by spark plasma sintering. The systematic comparison of the microstructural and transport properties of the Ref and MS samples evidences differences that can be ascribed to the peculiar microstructure achieved by MS. Although both series of samples are well crystallized, the chemical homogeneity is not equivalent. The SPS-processed ribbons yield bulk dense samples highly homogeneous while the reference samples exhibit some segregations at the microscale that might be due to the specific characteristics of the pseudo-binary Bi_2Te_3 – Sb_2Te_3 phase diagram. Variations in the chemical composition of the initial ingot has a significant influence on the transport properties of the final samples as revealed by our detailed transport property measurements. Our results are in line with recent investigations on melt-spun materials. A peak *ZT* value of 1.1 at 340 K was achieved in the MS $x = 0.48$ sample. Our results demonstrate that the MS technique is a powerful tool to produce polycrystalline samples with high thermoelectric performances and with a very good reproducibility from sample to sample.

Acknowledgement

V.O. would like to acknowledge the support of EDF through the CIFRE convention N°2011/1329. The authors acknowledge support through the "Contrat-Plan-Etat-Region" 2014-2020 ENARBATIM and MAT-DS.

Compliance with Ethical Standards:

Conflict of Interest: The authors declare that they have no conflict of interest.

References

1. *Thermoelectric Handbook: Macro to nano*, Ed. D.M. Rowe, Taylor & Francis (2005).

2. *Thermoelectrics for power generation*, Eds M. Nikitin, S. Skipidarov, IntechOpen (2016).

3. *Bringing thermoelectricity into reality*, Ed. P. Aranguren, IntechOpen (2018).

4. Goldsmid HJ in *Thermoelectric Refrigeration*; Plenum Press: New York (1964).

5. *Thermoelectrics and Its Energy Harvesting*, Ed. D. M Rowe, CRC Press: Boca Raton, FL (2012).

6. *Thermoelectric Bi_2Te_3 nanomaterials*, Eds O. Eibl, K. Nielsch, N. Peranio, F. Völklein, Wiley (2015).

7. Goldsmid J (2014) Bismuth telluride and its alloys as materials for thermoelectric generation. Materials 5:2577-2592.

8. Xie W, Tang X, Yan Y, Zhang Q, Tritt TM (2009) Unique nanostructures and enhanced thermoelectric performance of melt-spun BiSbTe alloys. Appl. Phys. Lett. 94:102111.

9. Fan S, Zhao J, Guo J, Yan Q, Ma J, Hng HH (2010) P-type $Bi_{0.4}Sb_{1.6}Te_3$ nanocomposites with enhanced figure of merit. Appl. Phys. Lett. 96:182104.

10. Xie W, He J, Kang HJ, Tang X, Zhu S, Laver M, Wang S, Copley JRD, Brown CM, Zhang Q, Tritt TM (2010) Identifying the specific nanostructures responsible for the high thermoelectric performance of $(Bi,Sb)_2Te_3$ nanocomposites. Nano Lett. 10:3283-3289.

11. Xie W, Wang S, Zhu S, He J, Tang X, Zhang Q, Tritt TM (2013) High performance Bi_2Te_3 nanocomposites prepared by single-element-melt-spinning spark-plasma sintering. J. Mater. Sci. 48:2745-2760.

12. Glazov VM, Yatmanov YV, Ivanova AB (1986) Structural features of alloys of the Bi-Te system, produced by ultrafast quenching of the liquid-state. Inorg. Mater. USSR 22:520-526.

13. Glazov VM, Yatmanov YV (1990) Features of the breakdown of semiconducting metastable solid-solutions of the systems BiSe(Te) and SbTe prepared by quenching from the liquid. Inorg. Mater. USSR 26:1965-1967.

14. Koukharenko E, Frety N, Shepelevich VG, Tedenac JC (2000) Thermoelectric Properties of Bi_2Te_3 Material Obtained by the Ultrarapid Quenching Process Route. J. Alloys Compd. 299:254–257.

15. Koukharenko E, Frety N, Shepelevich VG, Tedenac JC (2001) Electrical properties of $Bi_{2-x}Sb_xTe_3$ materials obtained by ultrarapid quenching. J. All. Comp. 327:1-4.

16. Horio Y, Yamashita H, Hayashi T (2004) Microstructure and crystal orientation of rapidly solidified (Bi,Sb)(2)(Te,Se)(3) alloys by the liquid quenching technique. Mat. Transactions, 45:2757-2760.

17. Zheng Y, Zhang Q, Su X, Xie H, Shu S, Chen T, Tan G, Yan Y, Tang X, Uher C, Snyder GJ (2014) Mechanically robust BiSbTe alloys with superior thermoelectric performance: A case study of stable hierarchical nanostructured thermoelectric materials. Adv. Energy Mater. 1401391.

18. Ohorodniichuk V, Dauscher A, Masschelein P, Candolfi C, Baranek P, Dalicieux P, Lenoir B (2016) Investigation of the nozzle diameter as a control parameter of the properties of melt-spun $Sb_{2-x}Bi_xTe_3$. J. Electron. Mater. 45:1419-1424.

19. Ohorodniichuk V, Candolfi C, Masschelein P, Baranek P, Dalicieux P, Dauscher A, Lenoir B (2016) Influence of preparation processing on the transport properties of melt-spun $Sb_{2-x}Bi_xTe_{3+y}$. J. Electron. Mater. 45:1561–1569.

20. Ohorodniichuk V, Dauscher A, Branco Lopez E, Migot S, Candolfi C, Lenoir B, Crystals (2017) 7:172–189.

21. Zheng Y, Tan G, Luo Y, Yan Y, Tang X (2017) Thermal stability of p-type BiSbTe alloys prepared by melt spinning and rapid sintering. Materials 10:617.

22. Deng R, Su X, Luo T, Li J, Liu W, Yan Y, Tang X (2018) Modulation of carrier concentration and microstructure for high performance $Bi_xSb_{2-x}Te_3$ thermoelectrics prepared by rapid solidification. J. Solid State Chem. 264:141-147.

23. Deng R, Su X, Zheng Z, Liu W, Yan Y, Zhang Q, Dravid V, Uher C, Kanatzidis MG, Tang X (2018) Thermal conductivity in $Bi_{0.5}Sb_{1.5}Te_{3+x}$ and the role of dense dislocation arrays at grain boundaries. Sci. Adv. 4:5606.

24. Yoon JS, Song JM, Rahman JU, Lee S, Seo WS, Lee KH, Kim S, Kim HS, Kim S, Shin WH (2018) High thermoelectric performance of melt-spun $Bi_xSb_{2-x}Te_3$ by synergistic effect of carrier tuning and phonon engineering. Acta Mater. 158:289-296.

25 Murmu PP, Kennedy, J, Suman S, Chong SV, Leveneur J, Storey J, Rubanov S, Ramanath G (2019) Multifold improvement of thermoelectric power factor by tuning bismuth and antimony in nanostructured n-type bismuth antimony telluride thin films. Mater. Design 163:107549.

26. Alleno E, Berardan D, Byl C, Candolfi C, Daou R, Decourt R, Guilmeau E, Hébert S, Hejtmanek J, Masschelein P, Ohorodnichuk V, Pollet M, Populoh S, Ravot D, Rouleau O, Soulier M (2015) A round robin test of the uncertainty on the measurement of the thermoelectric dimensionless figure of merit of $Co_{0.97}Ni_{0.03}Sb_3$. Rev. Sci. Inst. 86:011301.

27. Caillat T, Carle M, Perrin D, Scherrer H, Scherrer S (1992) Study of the ternary Bi-Sb-Te phase diagram. J. Phys. Chem. Solids 53:227-232.

28. Li G, Gadelrab KR, Souier T, Potapov PL, Chen G, Chiesa M (2012) Mechanical properties of $Bi_xSb_{2-x}Te_3$ nanostructured thermoelectric materials. Nanotechnol. 23:065703.

29. Caillat T, Gailliard L, Scherrer H, Scherrer S (1993) Transport properties analysis of single crystals grown by the traveling heater method. J. Phys. Chem. Solids 54:575-581.

30. Champness CH, Chiang PT, Parekh P (1965) Thermoelectric properties of Bi_2Te_3-Sb_2Te_3 alloys. Can. J. Phys. 43:653.

31. Testardi LR, Wiese JR (1961) Density anomalies in the Bi_2Te_3-Sb_2Te_3 system. Trans. Metall. Soc. AIME, 221:647-649.

32. Volotskii MP, Gudkin TS, Dashevskii ZM, Kaidanov VI, Sgibnev IV (1974) Investigation of complex structure of band edges and of mechanism of carrier scattering in Bi-Sb-Te single crystals. Soviet Phys. Semicond.-USSR 8:682-283.

33. Gerovac N, Snyder GJ, Caillat T (2002) Thermoelectric properties of n-type polycrystalline $Bi_xSb_{2-x}Te_3$ alloys,) Proceedings XXI Intern. Conf. Thermoelectrics, ICT02, IEEE, p. 31-34.

34. Stordeur M, Langhammer HT, Sobotta H, Riede V (1981) Valence band-structure of $(Bi_{1-x}Sb_x)_2Te_3$ single crystals. Phys. Stat. Sol. B 104:513-522.

35. Goldsmid HJ, Sharp JW (1999) Estimation of the thermal band gap of a semiconductor from Seebeck coefficient. J. Electron. Mater. 28:869-872.

36. Stölzer M, Stordeur M, Sobotta H, Riede V (1986) IR transmission investigations of $(Bi_{1-x}Sb_x)_2Te_3$ single crystals. Phys. Stat. Sol. (b) 138:259-266.

37. Süssmann H, Heiliger W (1989) Seebeck coefficient and electrical conductivity in p-$(Bi_{1-x}Sb_x)_2Te_3$ at room temperature. Phys. Stat. Sol. (a) 80:535-539.

38. Xie W, He J, Zhu S, Holgate T, Wang S, Tang X, Zhang Q, Tritt TM (2011) Investigation of the sintering pressure and thermal conductivity anisotropy of melt-spun spark-plasma-sintered $(Bi,Sb)_2Te_3$ thermoelectric materials. J. Mater. Res. 26:1791-1799.

39. Ebling DG, Jacquot A, Jägle M, Böttner H, Kühn U, Kirste L (2007) Structure and thermoelectric properties of nanocomposite bismuth telluride prepared by melt spinning or by partially alloying with IV-VI compounds. Phys. Stat. Sol. (RRL) 1:238-240.

40. Böttner H, Ebling DG, Jacquot A, Kühn U, Schmidt J (2008) Melt spinning preparation of bismuth telluride and partially alloying with IV-VI compounds for thermoelectric application. Mater. Res. Soc. Symp. Proc. 1044:U04-01.

41. Ivanova LD, Petrova LI, Granatkina YV, Leontyev VG, Ivanov AS, Varlamov SA, Prilepo YP, Sychev AM, Chuik AG, Bashkov IV (2013) Thermoelectric and Mechanical Properties of the $Bi_{0.5}Sb_{1.5}Te_3$ Solid Solution Prepared by Melt Spinning. Inorg. Mater. 49:120–126.

Tables

Table 1. Nominal and actual compositions in the four samples studied determined by WDXS. The actual chemical compositions have been obtained by averaging around 90 different measurement points and were calculated by normalizing the chemical formulae to 5 atoms per formula unit.

Sample	Nominal	Actual
Ref0.40	$Bi_{0.40}Sb_{1.60}Te_3$	$Bi_{0.42}Sb_{1.54}Te_{3.04}$
MS0.40	$Bi_{0.40}Sb_{1.60}Te_3$	$Bi_{0.40}Sb_{1.56}Te_{3.04}$
Ref0.48	$Bi_{0.48}Sb_{1.52}Te_3$	$Bi_{0.48}Sb_{1.47}Te_{3.05}$
MS0.48	$Bi_{0.48}Sb_{1.52}Te_3$	$Bi_{0.50}Sb_{1.44}Te_{3.06}$

Figure captions

Fig. 1. Sketch of the adopted scheme for cutting the samples parallel (red color) and perpendicular (blue color) to the pressing direction. Low temperature measurements: bar-shaped samples for both electrical and thermal properties cut in “perp” and “par” directions (PPMS, TTO), bar-shaped samples cut in “perp” direction for galvanomagnetic measurements (PPMS, ACT). High temperature measurements: bar-shaped samples for electrical properties (ZEM3); cylindrical (“par”) or square- (“perp”) shaped samples for thermal diffusivity measurements (LFA).

Fig. 2. PXRD patterns of the $Bi_xSb_{2-x}Te_3$ samples: a) reference and melt-spun samples for x = 0.40, b) magnification of the region around the (015) peak. The PXRD patterns of the Ref and MS x = 0.48 samples are similar and can be found in our prior study [20].

Fig. 3. a, b, c, d: backscattered electron images collected on polished samples; **e, f**: secondary electron images of fractured samples. The label of the sample is given on the images.

Fig. 4. Compositions determined by WDXS on roughly 100 points over the surface on reference and melt-spun samples for x = 0.40. The points have been sorted out as a function of increasing atomic Bi content. The black lines correspond to the expected composition. Open and filled samples refer to the reference and melt-spun samples, respectively.

Fig. 5. TEM images collected on the MS0.40 sample. a) Bright field (BF) image showing an agglomeration of small nano-particles. The corresponding electron diffraction pattern and dark field images highlighting (in white) the nano-crystals diffracting in the (015) (yellow) and (1010) (blue) Bragg positions. b) BF image of another fragment of the sample showing larger crystals and micro-electron diffraction pattern of a single crystal corresponding to the pink area.

Fig. 6. Temperature dependence of the electrical resistivity ρ for the (a) reference and (b) MS $Bi_xSb_{2-x}Te_3$ samples for x = 0.40 and 0.48. Measurements were performed parallel and perpendicular to the pressing direction.

Fig. 7. Temperature dependence of the Hall coefficient R_H for the (a) reference and (b) MS $Bi_xSb_{2-x}Te_3$ samples for x = 0.40 and 0.48. Measurements were performed parallel and perpendicular to the pressing direction.

Fig. 8. Temperature dependence of the hole concentration p for the (a) reference and (b) MS $Bi_xSb_{2-x}Te_3$ samples for x = 0.40 and 0.48.

Fig. 9. Temperature dependence of the Hall mobility μ_H for the (a) reference and (b) MS $Bi_xSb_{2-x}Te_3$ samples for x = 0.40 and 0.48. The solid black line shows the $T^{-3/2}$ dependence expected for purely acoustic phonon scattering.

Fig. 10. Temperature dependence of the thermopower S for the (a) reference and (b) MS $Bi_xSb_{2-x}Te_3$ samples for x = 0.40 and 0.48. Measurements were performed parallel and perpendicular to the pressing direction.

Fig. 11. Temperature dependence of the total thermal conductivity κ for the (a) reference and (b) MS $Bi_xSb_{2-x}Te_3$ samples for x = 0.40 and 0.48. Measurements were performed parallel and perpendicular to the pressing direction.

Fig. 12. Temperature dependence of *ZT* for the (a) reference and (b) MS $Bi_xSb_{2-x}Te_3$ samples for x = 0.40 and 0.48. Measurements were performed parallel and perpendicular to the pressing direction.

Fig. 13. Temperature dependence of the (a) electrical resistivity, (b) thermopower, (c) hole concentration, (d) Hall mobility, (e) total thermal conductivity and (f) *ZT* of two different batches of MS $Sb_{1.52}Bi_{0.48}Te_3$ samples. Measurements were performed parallel and perpendicular to the pressing direction.

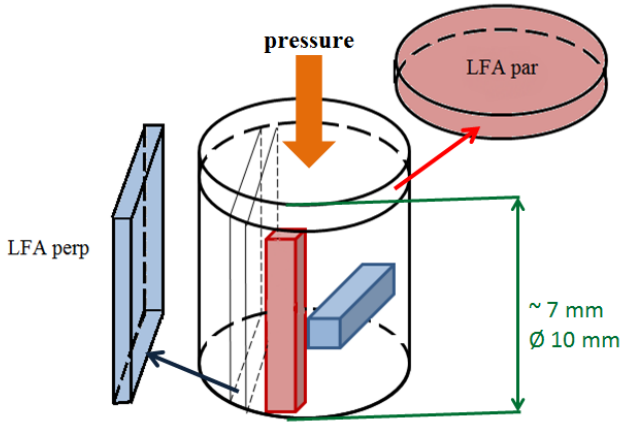

Figure 1

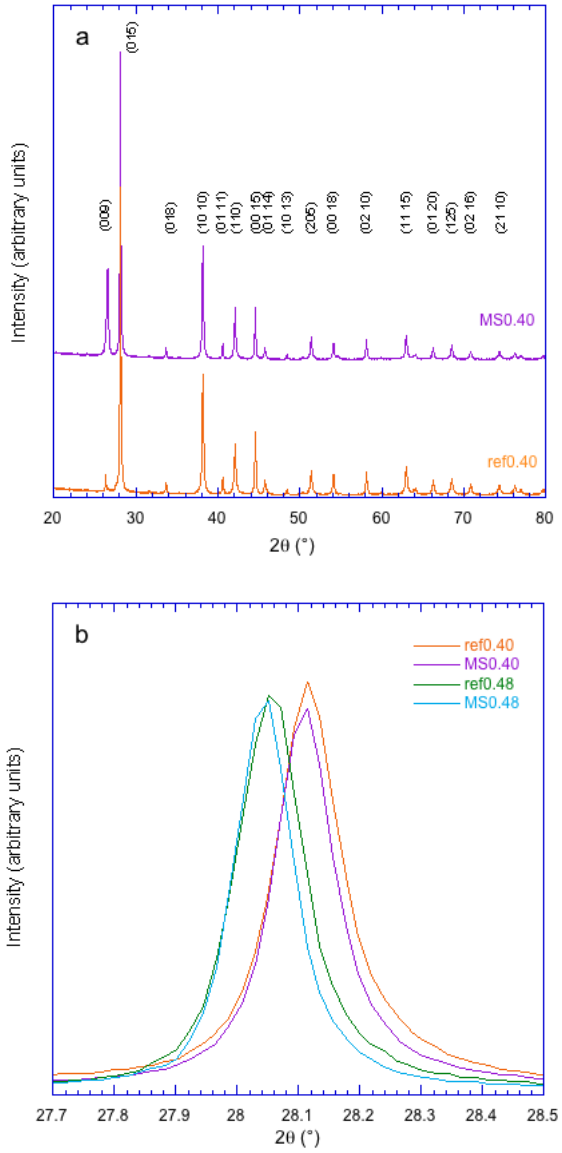
a
(009)
(015)
(018)
(10 10)
(01 11)
(110)
(00 15)
(01 14)
(10 13)
(205)
(00 18)
(02 10)
(11 15)
(01 20)
(125)
(02 16)
(21 10)
MS0.40
ref0.40
Intensity (arbitrary units)
20
30
40
50
60
70
80
2θ (°)
b
ref0.40
MS0.40
ref0.48
MS0.48
Intensity (arbitrary units)
27.7
27.8
27.9
28
28.1
28.2
28.3
28.4
28.5
2θ (°)

Figure 2

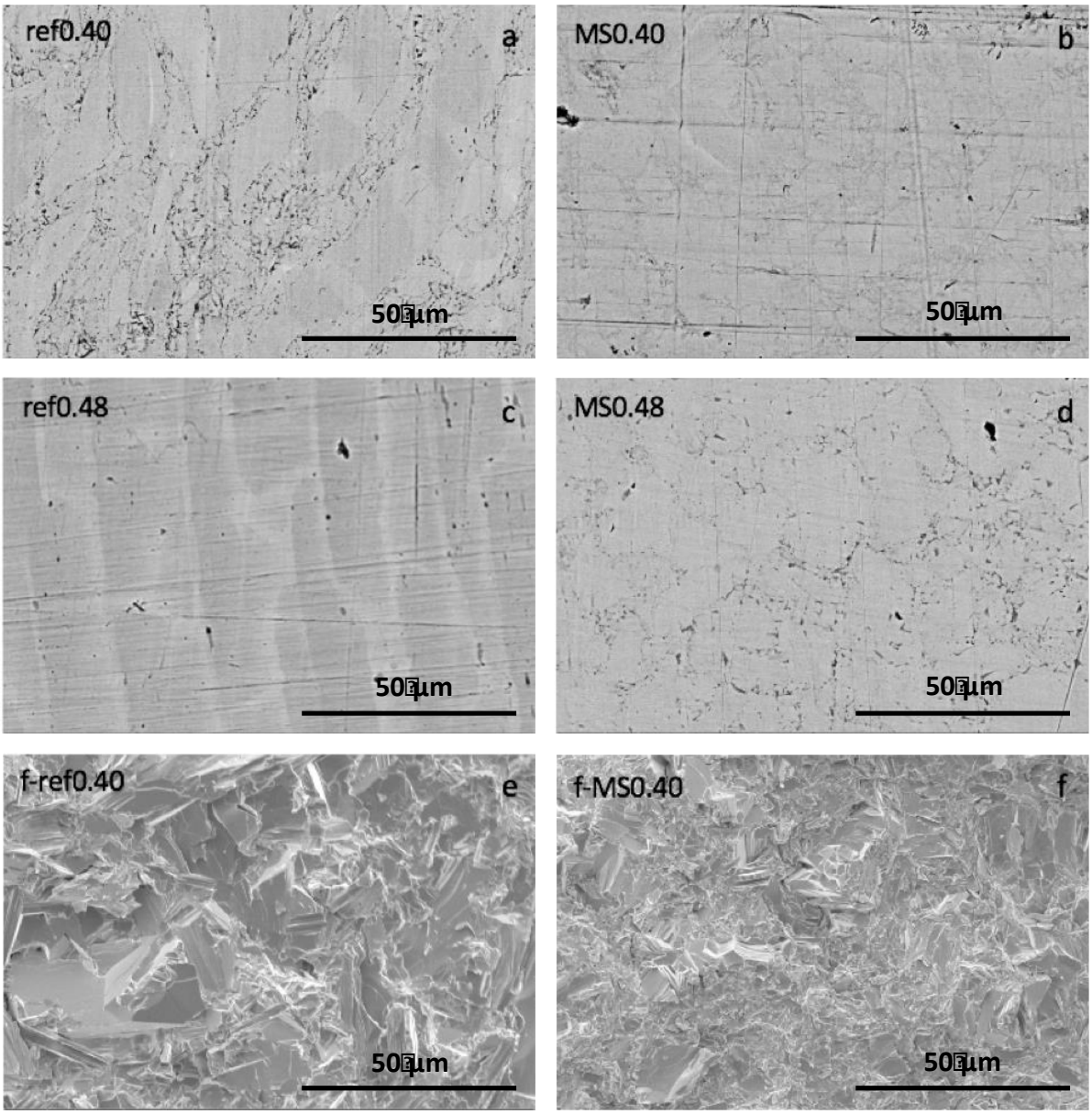
ref0.40
a
50 µm
MS0.40
b
50 µm
ref0.48
c
50 µm
MS0.48
d
50 µm
f-ref0.40
e
50 µm
f-MS0.40
f
50 µm

Figure 3

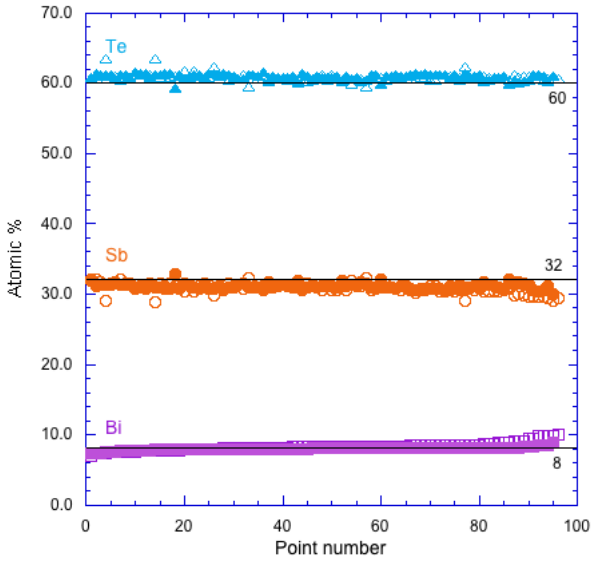
70.0
60.0
50.0
40.0
30.0
20.0
10.0
0.0
Atomic %
Te
60
Sb
32
Bi
8
0
20
40
60
80
100
Point number

Figure 4

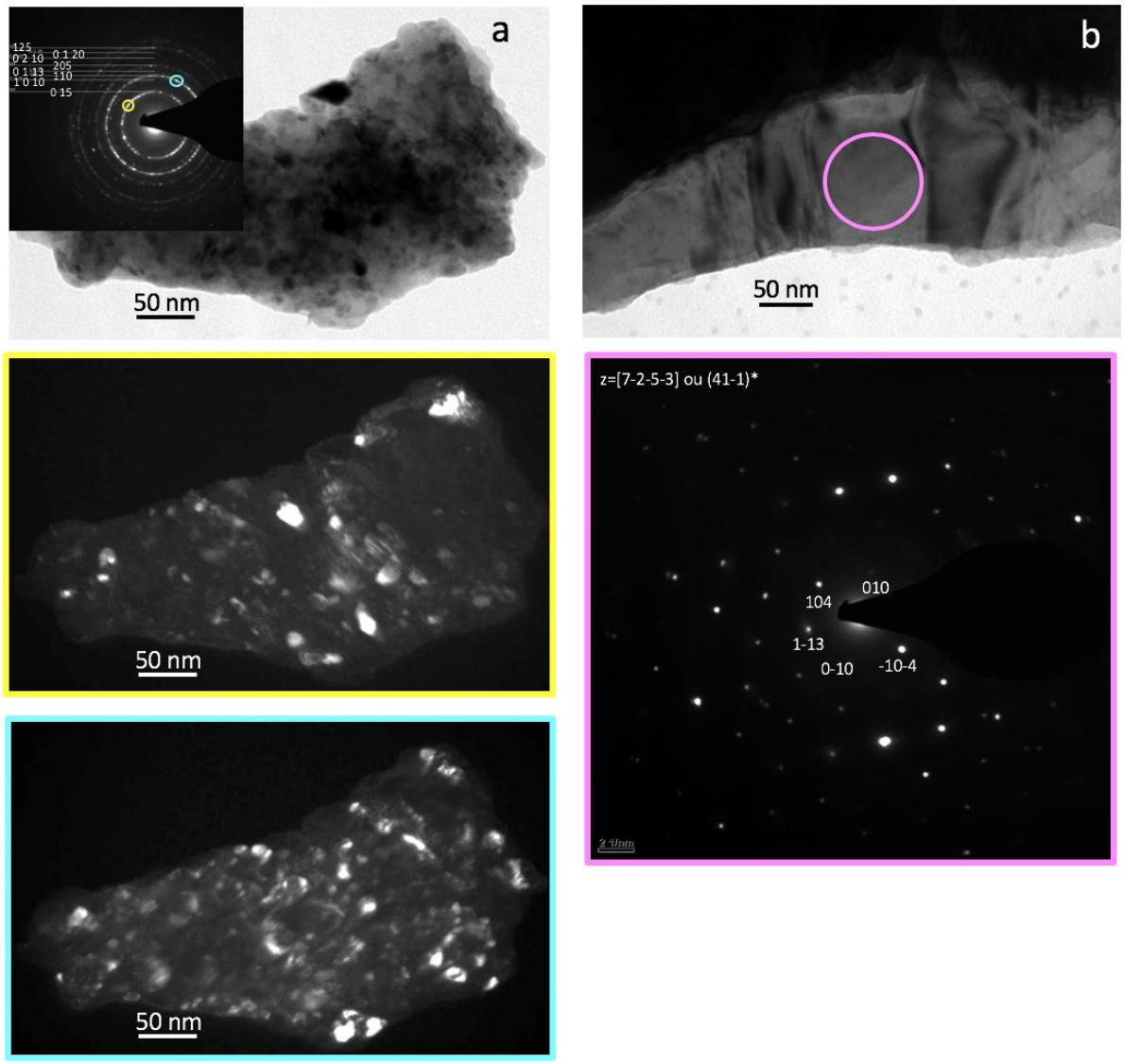

Figure 5

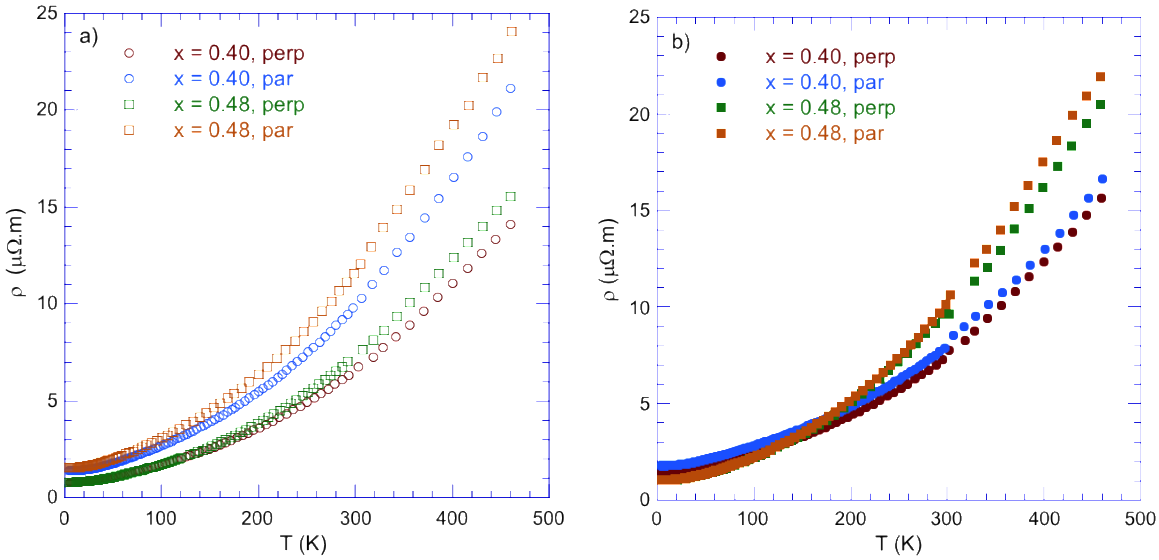

Figure 6

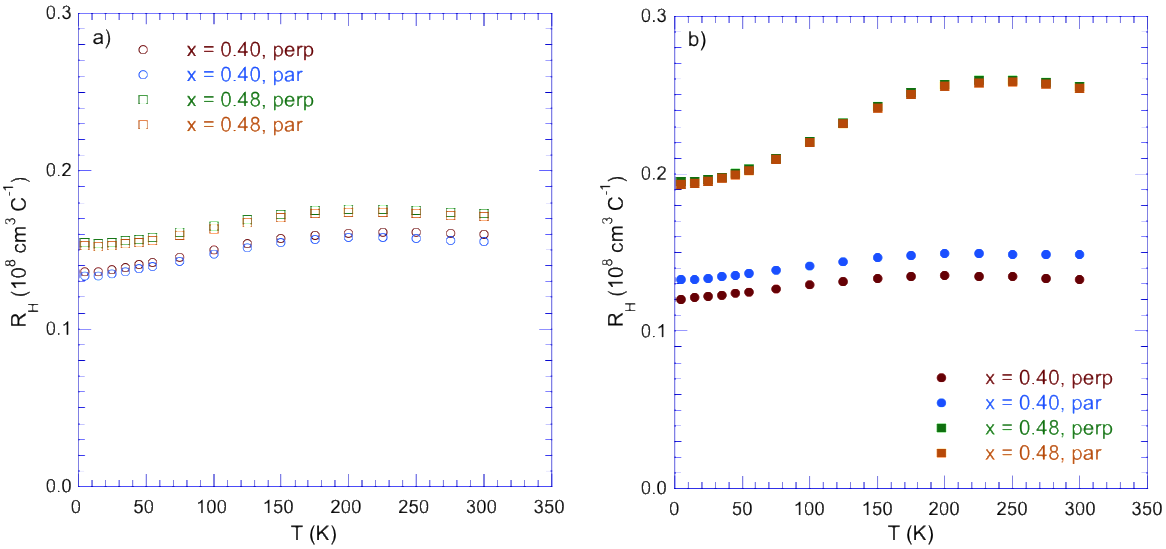

Figure 7

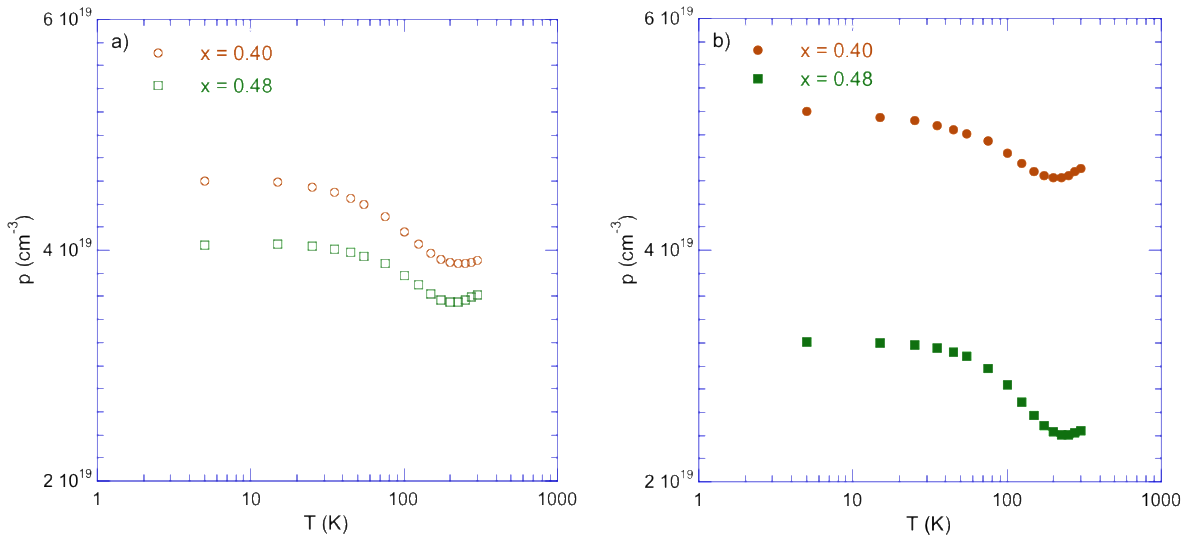

Figure 8

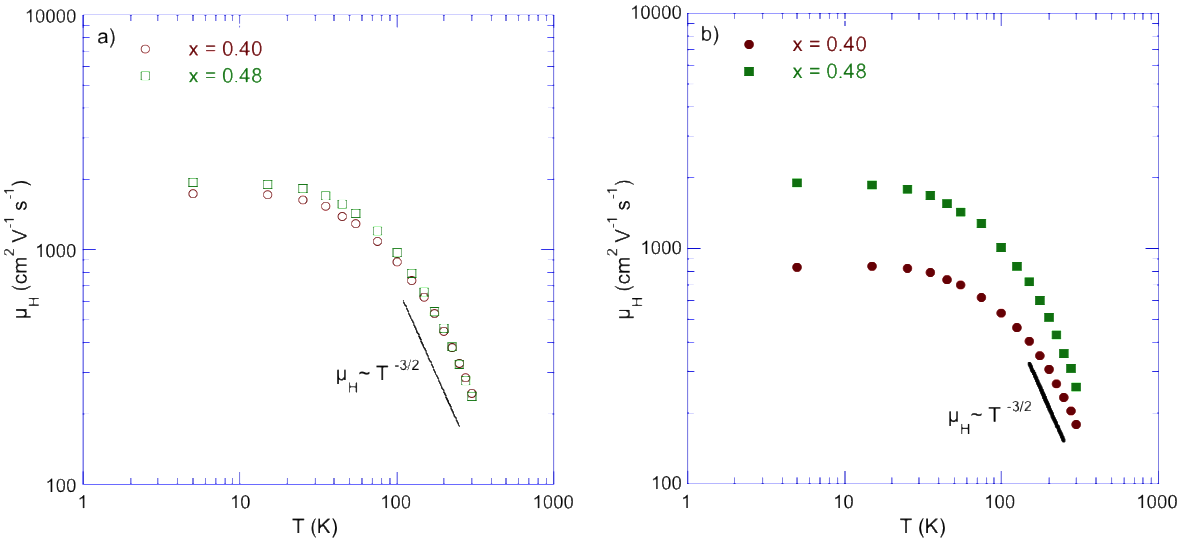

Figure 9

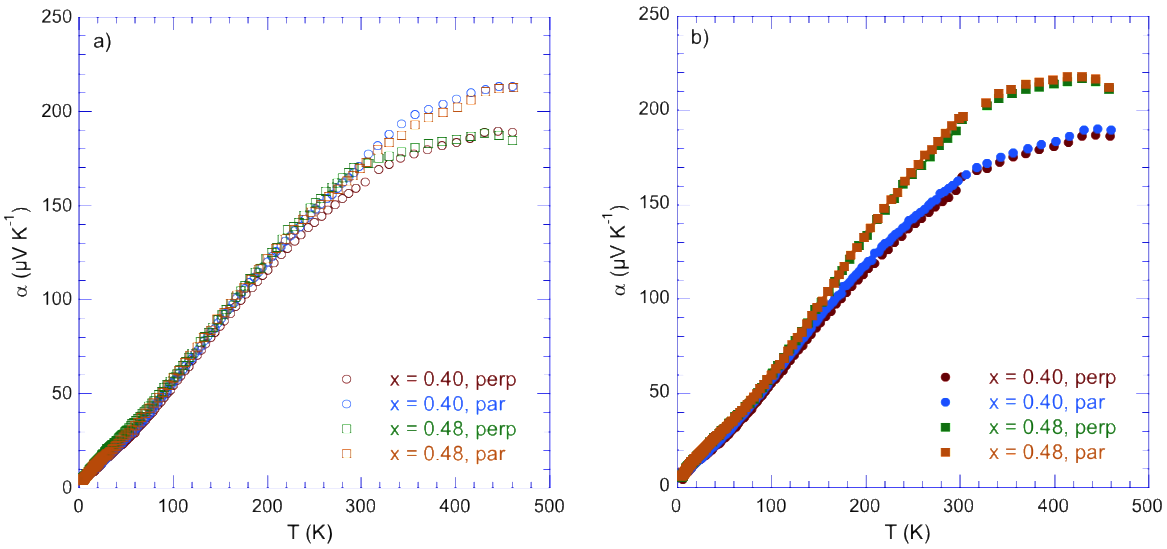

Figure 10

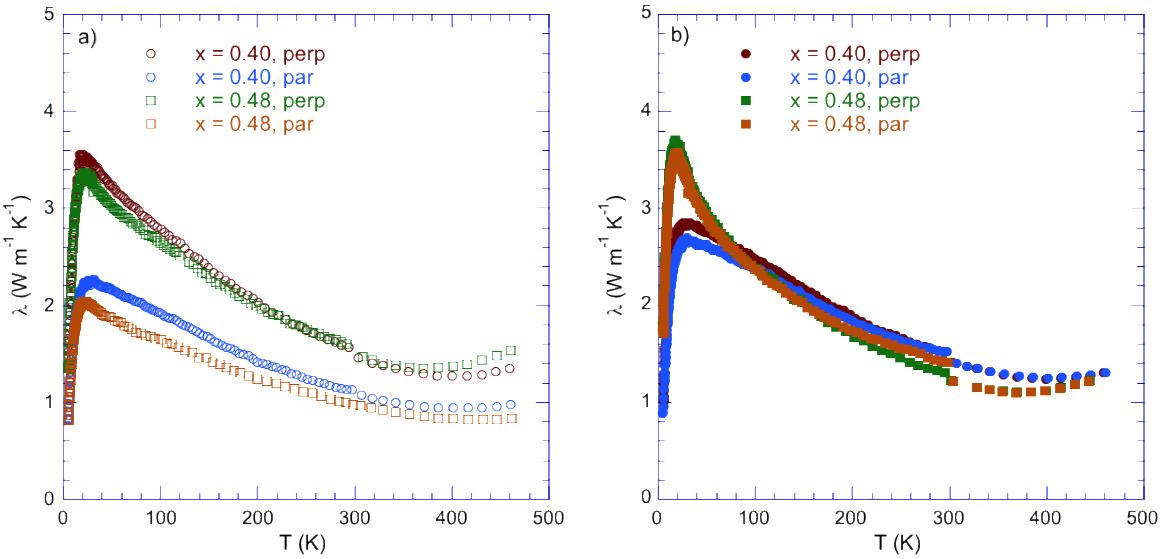

Figure 11

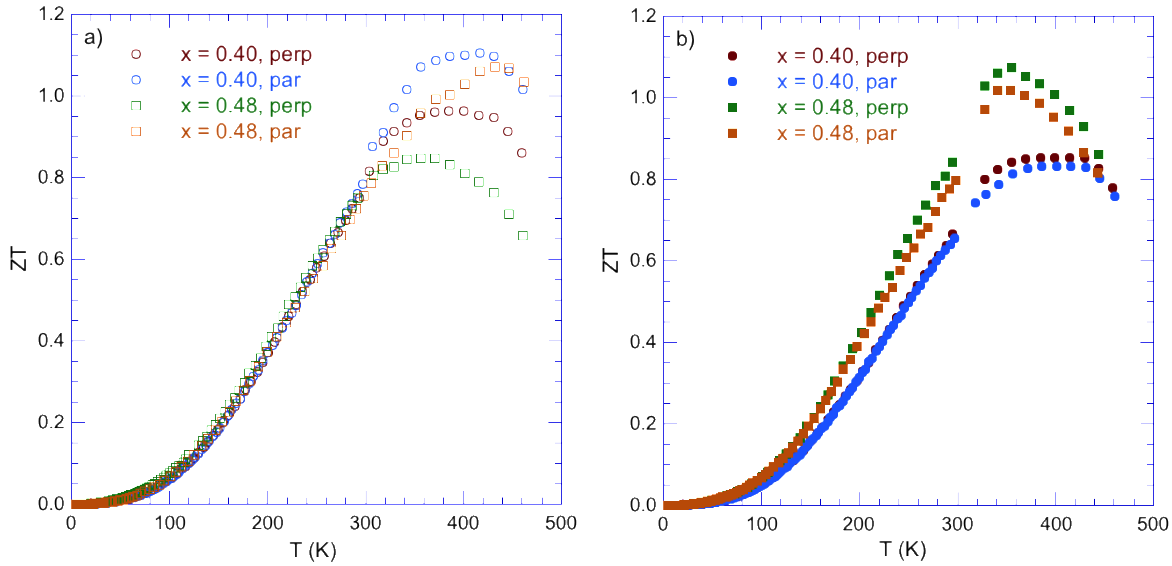
a)
x = 0.40, perp
x = 0.40, par
x = 0.48, perp
x = 0.48, par
ZT
T (K)
b)
x = 0.40, perp
x = 0.40, par
x = 0.48, perp
x = 0.48, par
ZT
T (K)

Figure 12

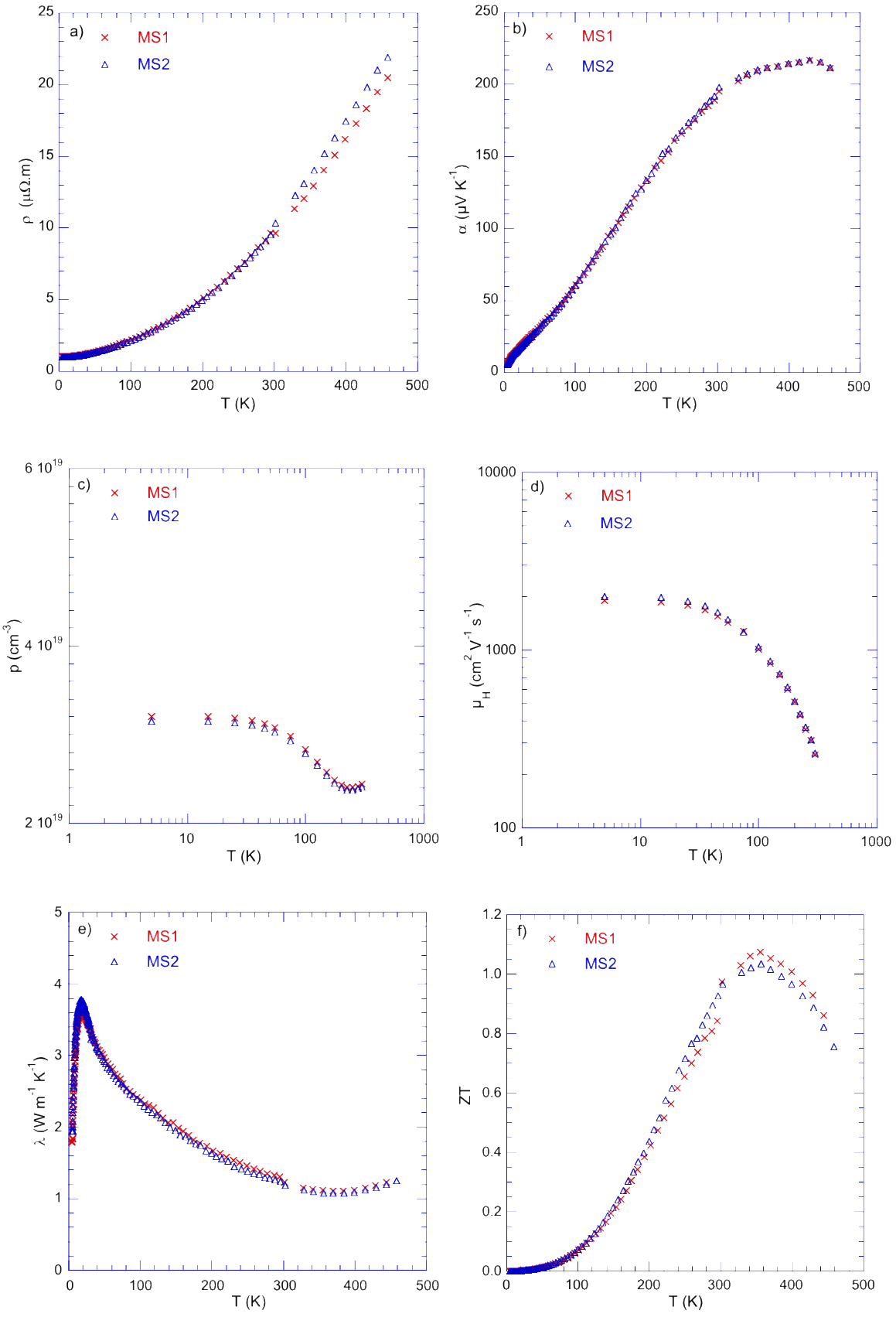
a)
MS1
MS2
ρ (μΩ.m)
T (K)
b)
MS1
MS2
α (μV K-1)
T (K)
c)
MS1
MS2
p (cm-3)
T (K)
d)
MS1
MS2
μH (cm2 V-1 s-1)
T (K)
e)
MS1
MS2
λ (W m-1 K-1)
T (K)
f)
MS1
MS2
ZT
T (K)

Figure 13